



Originally published as:

Schneider, F. M., Yuan, X., Schurr, B., Mechie, J., Sippl, C., Kufner, S.-K., Ratschbacher, L., Tilmann, F., Oimahmadov, I., Gadoev, M., Minaev, V., Abdybachaev, U., Orunbaev, S., Ischuk, A., Murodkulov, S. (2019): The Crust in the Pamir: Insights from Receiver Functions. - *Journal of Geophysical Research*, 124, 8, pp. 9313—9331.

DOI: <http://doi.org/10.1029/2019JB017765>



## RESEARCH ARTICLE

10.1029/2019JB017765

## The Crust in the Pamir: Insights From Receiver Functions

F.M. Schneider<sup>1</sup> , X. Yuan<sup>1</sup>, B. Schurr<sup>1</sup> , J. Mechie<sup>1</sup> , C. Sippl<sup>1,5</sup> , S.-K. Kufner<sup>1</sup> , L. Ratschbacher<sup>2</sup> , F. Tilmann<sup>1,6</sup> , I. Oimahmadov<sup>3</sup>, M. Gadoev<sup>3</sup> , V. Minaev<sup>3</sup> , U. Abdybaev<sup>4</sup>, S. Orunbaev<sup>4</sup>, A. Ischuk<sup>3</sup>, and S. Murodkulov<sup>3</sup>

## Key Points:

- Double normal crustal thickness of 65–75 km underneath the Pamir and Hindu Kush transitions to ~40 km below the surrounding basins
- Double Moho beneath the Central and western South Pamir indicates that Tajik/Tarim continental crust underlies Pamir crust
- Low  $V_p/V_s$  in South and Central Pamir crust suggests bulk felsic composition due to delamination/foundering of the mafic lower crust

## Supporting Information:

- Supporting information S1
- Data Set S1

## Correspondence to:

F. M. Schneider,  
felix@gfz-potsdam.de

## Citation:

Schneider, F. M., Yuan, X., Schurr, B., Mechie, J., Sippl, C., Kufner, S.-K., et al. (2019). The crust in the Pamir: Insights from receiver functions. *Journal of Geophysical Research: Solid Earth*, 124, 9313–9331. <https://doi.org/10.1029/2019JB017765>

Received 29 MAR 2019

Accepted 2 AUG 2019

Accepted article online 7 AUG 2019

Published online 22 AUG 2019

<sup>1</sup>Deutsches GeoForschungsZentrum - GFZ, Potsdam, Germany, <sup>2</sup>Institut für Geologie, Technische Universität Bergakademie Freiberg, Freiberg, Germany, <sup>3</sup>Institute of Geology, Earthquake Engineering and Seismology, Academy of Sciences of the Republic of Tajikistan, Dushanbe, Tajikistan, <sup>4</sup>Central Asian Institute for Applied Geosciences, Bishkek, Kyrgyzstan, <sup>5</sup>Now at Institute of Geophysics, Czech Academy of Sciences, Prague, Czech Republic, <sup>6</sup>Department of Earth Sciences, Freie Universität Berlin, Berlin, Germany

**Abstract** The Cenozoic convergence between India and Asia has created Earth's thickest crust in the Pamir-Tibet Plateau by extreme crustal shortening. Here we study the crustal structure of the Pamir and western Tian Shan, the adjacent margins of the Tajik, Tarim, and Ferghana Basins, and the Hindu Kush, using data collected by temporary seismic experiments. We derive, compare, and combine independent observations from *P* and *S* receiver functions. The obtained Moho depth varies from ~40 km below the basins to a double-normal thickness of 65–75 km underneath the Pamir and Hindu Kush. A Moho doublet—with the deeper interface down to a depth of ~90 km—coincides with the arc of intermediate-depth seismicity underneath the Pamir, where Asian continental lower crust delaminates and rolls back. The crust beneath most of the Central and South Pamir has a low  $V_p/V_s$  ratio (<1.70), suggesting a dominantly felsic composition, probably a result of delamination/foundering of the mafic rocks of the lower crust. Beneath the Cenozoic gneiss domes of the Central and South Pamir, which represent extensional core complexes, the  $V_p/V_s$  ratios are moderate to high (~1.75), consistent with the previously observed, midcrustal low-velocity zones, implying the presence of crustal partial melts. Even higher crustal average  $V_p/V_s$  ratios up to 1.90 are found in the sedimentary basins and along the Main Pamir Thrust. The ratios along the latter—the active thrust front of the Pamir—may reflect fluid accumulations within a strongly fractured fault system.

## 1. Introduction

The Pamir has been forming at the northwestern tip of the India-Asia collision zone since ~50 Ma (e.g., Najman et al., 2010) and, together with the Tibet Plateau, contains the thickest crust on Earth (e.g., Reguzzoni et al., 2013; Figure 1). To infer the geodynamic processes that created the thick crust, detailed information on the present-day crustal structure is essential. Specifically, mapping the crustal thickness and structure of the Pamir and its surrounding basins may provide constraints for assessing the role of continental subduction, crustal recycling into the mantle, and lateral extrusion of crust out of the orogen, when considered alongside geological evidence for strong shortening across the Pamir.

Although previous studies mostly based on satellite gravity observations showed that the Pamir has a continental crustal thickness of twice the global average, detailed information on the thickness and bulk composition based on local seismic data is missing. Steffen et al. (2011) obtained a map of crustal thickness for Central Asia including the Tian Shan and the Pamir by modeling the EGM2008 gravity data. Reguzzoni et al. (2013) combined a global seismic crustal model (CRUST2.0) with satellite gravity data and improved the standard deviation of the seismic crustal model at places where seismic data are sparse. Robert et al. (2017) obtained a crustal thickness map of Central Asia by combining elevation, geoid anomaly, and thermal data. These studies imply a crustal thickness of up to 75 km in the Pamir and Tian Shan, but with low spatial resolution (>0.5°) and without detailed information on the crustal structure and composition.

In Soviet times, a number of controlled-source, wide-angle seismic profiles were acquired and evaluated, covering parts of the southern Tian Shan, Tajik Basin, and Pamir. A crustal thickness of 50–55 km was found beneath the Ferghana Basin and southern Tian Shan; it increases to 70–75 km beneath the North Pamir and decreases to 60–65 km beneath the Central and South Pamir (Belousov et al., 1980). Beneath the Tajik

© 2019. The Authors.

This is an open access article under the terms of the Creative Commons Attribution License, which permits use, distribution and reproduction in any medium, provided the original work is properly cited.

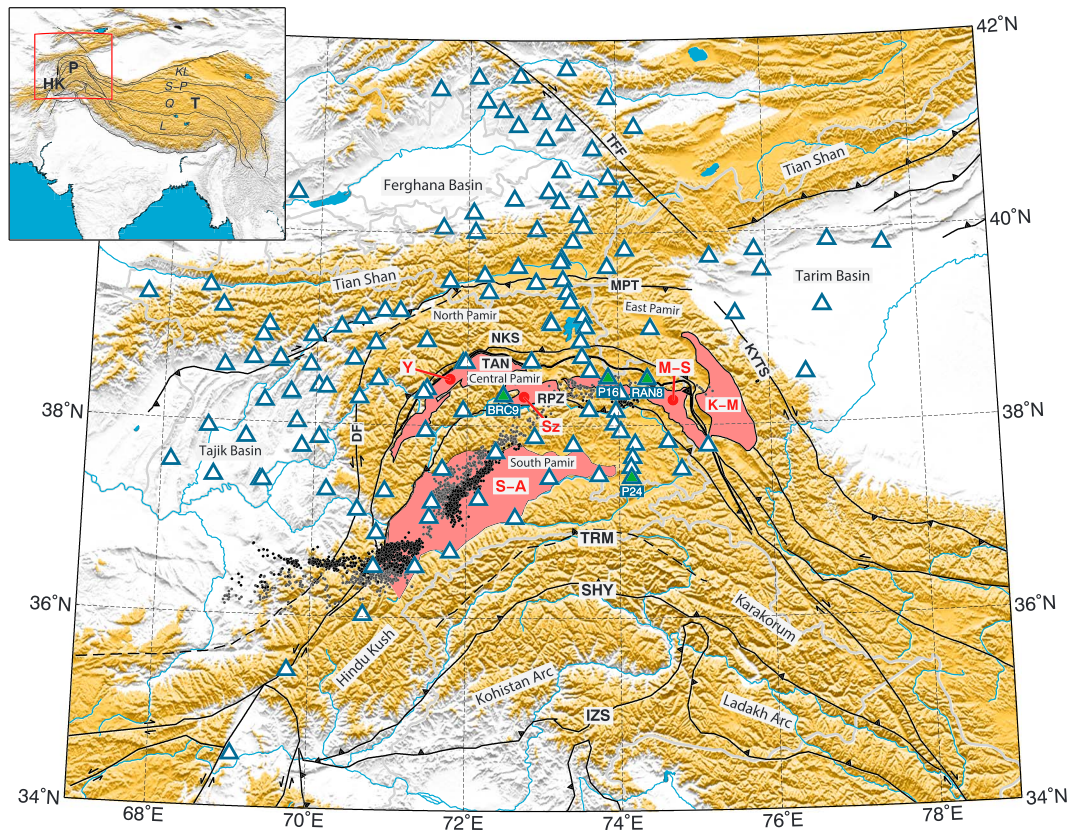


**Figure 1.** Map showing the geological features and locations of the seismic stations (blue triangles). Green-filled triangles mark stations for which data are shown in Figures 3 and 9. Sutures and faults are modified after Robinson et al. (2004) and Kufner, Schurr, et al. (2018) from north to south: Talas-Ferghana Fault (TFF), Main Pamir Thrust (MPT), North Pamir/Kunlun Suture (NKS), Kashgar-Yencheng Transfer System (KYTS), Tanymas Suture (TAN), Rushan-Pshart Zone (RPZ), Darvaz Fault (DF), Tirich-Mir Zone (TRM), Shyok Suture (SHY), and Indus-Zangbo Suture (IZS). Red shaded areas mark the Cenozoic gneiss domes of the Pamir: Yazgulom (Y), Sarez (Sz), Muskol-Shatput (M-S), Kongur Shan-Muztaghata (K-M), Shakhdara-Alichur (S-A). Grey and black dots are the earthquake epicenters from Kufner et al. (2016) with focal depths in the 100–150- and 150–300-km ranges, respectively. Inset shows the Indian-Asian collision zone: Hindu-Kush (HK), Pamir (P), and Tibet (T). Terranes are Kunlun (KL), Songpan-Ganzi (S-G), Qiangtang (Q), and Lhasa (L). Altitudes exceeding 3,000 m are highlighted in brown, including Tibet, Himalaya, Pamir, and the Tian Shan.

Basin, crustal thickness values between ~37 and 49 km were obtained (Burtman & Molnar, 1993; Kulagina et al., 1974). However, these investigations suffer from insufficient publication, documentation, and justification of data analysis (see comments in Burtman & Molnar, 1993).

Since 2008, temporary local seismic arrays have been operated in the Pamir and surrounding regions. In the course of this work, Mechie et al. (2012) detailed the crustal structure and thickness along a north-south profile traversing the Pamir by wide-angle reflections and refractions observed from local earthquakes. The crustal thickness obtained in this study varies from ~58 km in the North Pamir, through ~74 km in the Central Pamir, to ~66 km in the South Pamir. The  $P$  wave velocity was shown to be relatively low (<6.3 km/s) with respect to the global average. Moreover, they inferred a low average crustal Poisson's ratio (0.23, corresponding to a  $V_p/V_s$  ratio of 1.69) in the Central and South Pamir. Schneider et al. (2013) used the same transect to construct receiver function cross sections showing similar crustal thickness variations, except for a slightly deeper Moho in the South Pamir. Furthermore, they resolved a south dipping, ~15-km-thick, low-velocity zone, interpreted as delaminating or subducting Asian lower crust.

In this paper, we study the crustal structure and map the crustal thickness and  $V_p/V_s$  ratio beneath the seismic arrays using converted seismic waves and their multiples. Our results are in general agreement with the previous studies, but provide information over a broader area of the Pamir and the surrounding regions. The detailed maps of the Moho depth and crustal  $V_p/V_s$  ratio are used to constrain the mode of crustal convergence and to infer the recent geodynamic evolution of the Pamir.

## 2. Tectonic Setting

The Pamir of Central Asia constitutes the northwestern extension of the Tibet Plateau. In the north, west, east, and south, it abuts, respectively, on the western Tian Shan, Tajik Basin, Tarim Basin, and the Hindu Kush and Karakorum (Figure 1). The Pamir consists of a similar amalgamation of lithospheric terranes as Tibet. These terranes, comprising Gondwana-derived microcontinents, subduction-accretion complexes, and arcs, were accreted to Asia during the Paleozoic and Mesozoic (e.g., Robinson et al., 2012; Schwab et al., 2004) and are nowadays separated by roughly east-west trending suture zones. In the Pamir, the intervening sutures are the North Pamir-Kunlun Suture, the Tanyamas suture, and the Rushan-Pshart Zone; they outline an orocline and are the basis for the classic subdivision into the North, Central, and South Pamir. Compared to Tibet, the North Pamir correlates to the Kunlun and Songpan-Ganzi terranes, and the Central and South Pamir as well as the Hindu Kush and Karakorum to the Qiangtang and Lhasa terranes (e.g., Robinson et al., 2012; Schwab et al., 2004). The lithosphere of the amalgamated Gondwana terranes likely was weakened rheologically by the long history of subduction, accretion, arc formation, and tectonism (e.g., Angiolini et al., 2013; Kufner et al., 2016; Schwab et al., 2004). Cenozoic relative northward motion of the Pamir with respect to its surrounding basins has mostly been accommodated along the Darvaz fault in the west and the Kashgar-Yencheng Transfer System in the east (Cowgill, 2010). Most of the current crustal N-S shortening is accommodated along the Main Pamir Thrust (Kufner, Schurr, et al., 2018; Schurr et al., 2014) by periodically occurring large earthquakes (Sippl et al., 2014).

The Central and South Pamir crust experienced Cenozoic high-grade metamorphism and magmatism. The related rock outcrop in extensional gneiss domes; the Shakhdara dome in the South Pamir; the Yazgulom, Sarez, Muskol, and Shatput domes in the Central Pamir; and the Kongur Shan and Muztaghata domes in the East Pamir of China (Figure 1). The Cenozoic mineral assemblages indicate Barrovian-facies metamorphism, which culminated in regional migmatization in the Shakhdara dome and anatectic plutonism in all domes (e.g., Chapman et al., 2018; Grew et al., 1994; Hacker et al., 2017; Peykre et al., 1981; Robinson et al., 2004; Schmidt et al., 2011). These gneiss domes collectively make up ~20% of the exposed rock of the Pamir, having surface areas of ~2,000–30,000 km<sup>2</sup>.

Clastic and carbonate metasedimentary sequences dominate the Central Pamir, but also include large volumes of Paleozoic to Miocene quartzofeldspathic orthogneiss and granitoids (Hacker et al., 2017; Rutte, Ratschbacher, Schneider, et al., 2017; Rutte, Ratschbacher, Khan, et al., 2017; Schwab et al., 2004). Quartzofeldspathic plutonic rocks of the Jurassic-Cretaceous, Andean-style magmatic arc, and its Proterozoic-Mesozoic host rocks along the southern margin of Asia dominate the South Pamir (Hacker et al., 2017; Stübner, Ratschbacher, Rutte, et al., 2013; Stübner, Ratschbacher, Weise, et al., 2013). Structural investigations reveal that the Central Pamir domes formed in crust that was tripled in thickness by north-south shortening during the late Eocene-Oligocene (Rutte, Ratschbacher, Schneider, et al., 2017; Rutte, Ratschbacher, Khan, et al., 2017). This implies that the crust was thicker than the present 60–70-km-thick Pamir crust (Mechie et al., 2012). Mostly Miocene, syn-convergent exhumation along large-scale, normal-sense shear zones exhumed the mostly felsic crust from 25- to 50-km depth in the gneiss domes of the Central and South Pamir. Exhumation was likely driven by the sudden removal of crustal compressive forces when the underthrusting Indian slab broke off (Rutte, Ratschbacher, Khan, et al., 2017; Stearns et al., 2013, 2015).

The Pamir and Hindu Kush host a zone of intermediate-depth seismicity down to ~300 km (Kufner et al., 2016, 2017; Sippl, Schurr, Yuan, et al., 2013). In map view, this intermediate-depth seismic zone forms an ~450-km-long band from the Hindu Kush in northeastern Afghanistan to the East Pamir of China (Figure 1). Beneath the Pamir and the Hindu Kush, the hypocenters of these earthquakes form two separated continental Wadati-Benioff zones (e.g., Burtman & Molnar, 1993; Fan et al., 1994; Pegler & Das, 1998). While north-south cross sections revealed opposite dips for both zones, accurate earthquake locations constrained the detailed geometry of the seismicity in the Pamir as a curvilinear arc, dipping to the south in the East Pamir and bending to an eastward dip beneath the southwestern South Pamir (Figure 1; Kufner et al., 2017; Sippl, Schurr, Yuan, et al., 2013). At the southwestern end of the arc, the intermediate-depth seismic zone dips due east and reaches ~240-km depth. At the eastern end, the deepest earthquakes occur at ~150-km depth. At depths below 80 km, the seismic zone beneath the Hindu Kush is spatially separated from the Pamir zone and hosts earthquakes with focal depths of up to 300 km.

Several scenarios were proposed to explain the different dips of the intermediate-depth seismic zones beneath the Hindu Kush and the Pamir. The two-slab scenario implies that the seismicity beneath the Pamir is situated within south and east dipping Asian crust, while the seismicity beneath the Hindu Kush occurs in northward subducting crust of Indian origin (Burtman & Molnar, 1993; Chatelain et al., 1980; Fan et al., 1994; Negredo et al., 2007; Roecker, 1982). One-slab scenarios locate the intermediate-depth seismicity beneath the Pamir and Hindu Kush in a single contorted slab of either Indian (Billington et al., 1977; Pavlis & Das, 2000; Pegler & Das, 1998) or Asian origin (Perry et al., 2019).

Recent studies of the intermediate-depth earthquakes and teleseismic tomography using local seismic arrays revealed an arcuate east to south dipping configuration for the Pamir seismic zone (Sippl, Schurr, Yuan, et al., 2013) and a north dipping seismic zone beneath the Hindu Kush (Kufner et al., 2016, 2017). Receiver function images (Schneider et al., 2013) showed that between ~70- and 90-km depth in the Pamir seismic zone, where there are no earthquakes, the Asian slab continuously dips to the south. In the upper mantle beneath the eastern Central Pamir, a 10–15-km-thick layer of Asian continental crust, descending to a depth of ~150 km, was observed hosting the intermediate-depth seismicity. This was confirmed by local earthquake tomography (Sippl, Schurr, Tympel, et al., 2013) and the observation of guided waves (Mechie et al., 2019). Together, these seismic observations demonstrate an east to south dipping slab of Asian lithosphere beneath the Pamir, which is corroborated by the observation of a clear deformation front along the Main Pamir Thrust (e.g., Burtman & Molnar, 1993; Zubovich et al., 2016). Sippl, Schurr, Tympel, et al. (2013) and Kufner et al. (2016) inferred that indenting cratonic Indian mantle lithosphere causes the arcuate shape of the Asian slab, delaminating, rolling back, and tearing apart the cratonic lithosphere of the Tajik/Tarim Basins underneath the Pamir.

The observation of a low-velocity zone beneath the Hindu Kush reaching down to a depth of ~160 km has been interpreted as subducted crust (Kufner et al., 2017; Li et al., 2018; Roecker, 1982). Tomographic images (Koulakov, 2011; Kufner et al., 2016) showed that a high-velocity zone, interpreted as a cold lithospheric slab, reaches down to ~600-km depth, thus much deeper than the seismicity beneath the southwestern edge of the Pamir and beneath the Hindu Kush. Koulakov (2011) described the shape of the deep-reaching lithosphere as a structure resembling a honey drop, originating from delamination rather than subduction. Molnar and Bendick (2019) similarly interpreted the observations of deep seismicity and the inference of a sinking lithospheric “blob” beneath the Hindu Kush to be caused by a Rayleigh-Taylor-type instability as GPS measurements north and south of the Hindu Kush show little relative shortening (Perry et al., 2019). In contrast, Kufner et al. (2016, 2017) derived from moment tensor inversion of the deep seismicity a stress state of vertical tension, which they interpreted together with the observation of a neck in the lithospheric slab as active slab break-off and thinning of subducting Indian lithosphere. Furthermore, they showed that the zone of intermediate-depth seismicity dips north; that is, it connects southward with Indian lithosphere, and the high-velocity zone outlines a slab. Taking the ~34-mm/year India-Asia convergence rates of Molnar and Stock (2009) and the length of the (restored) Indian and Asian slabs (380–400 km), the collision of the cratonic Indian and the cratonic Asian lithospheres would have started at 12–11 Ma (Kufner et al., 2016).

Miocene granulite- and eclogite-facies xenoliths from the southeastern Pamir provide a snapshot of what may have happened to the Pamir crust before the collision between the Asian and Indian lithospheres beneath the Pamir (Kooijman et al., 2017; Shaffer et al., 2017). The xenoliths were derived from mixed sedimentary-igneous Pamir crust like that exposed in the gneiss domes. At 14–11 Ma, the xenoliths were heated by 200–300 °C, buried to depths of ~90 km at rates of ~1 cm/year, that is, ~20 km below the present Moho, and invaded by ultrapotassic/carbonatitic melt. Shaffer et al. (2017) interpreted this to reflect crustal foundering, synchronous with the onset of Indian cratonic lithosphere indentation, causing rollback of the Asian cratonic lithosphere as inferred from the seismic imaging. The melting of the foundered crust and surrounding mantle produced the Neogene and younger (ultra)potassic magmatism of the South Pamir and adjacent Tibet, including the eruption of the xenoliths.

### 3. Data and Method

This work is based on teleseismic waveform data recorded by three temporary seismic networks, TIPAGE (Yuan et al., 2008), TIPTIMON (Schurr et al., 2012, 2013), and FERGHANA (Haberland et al., 2011), and

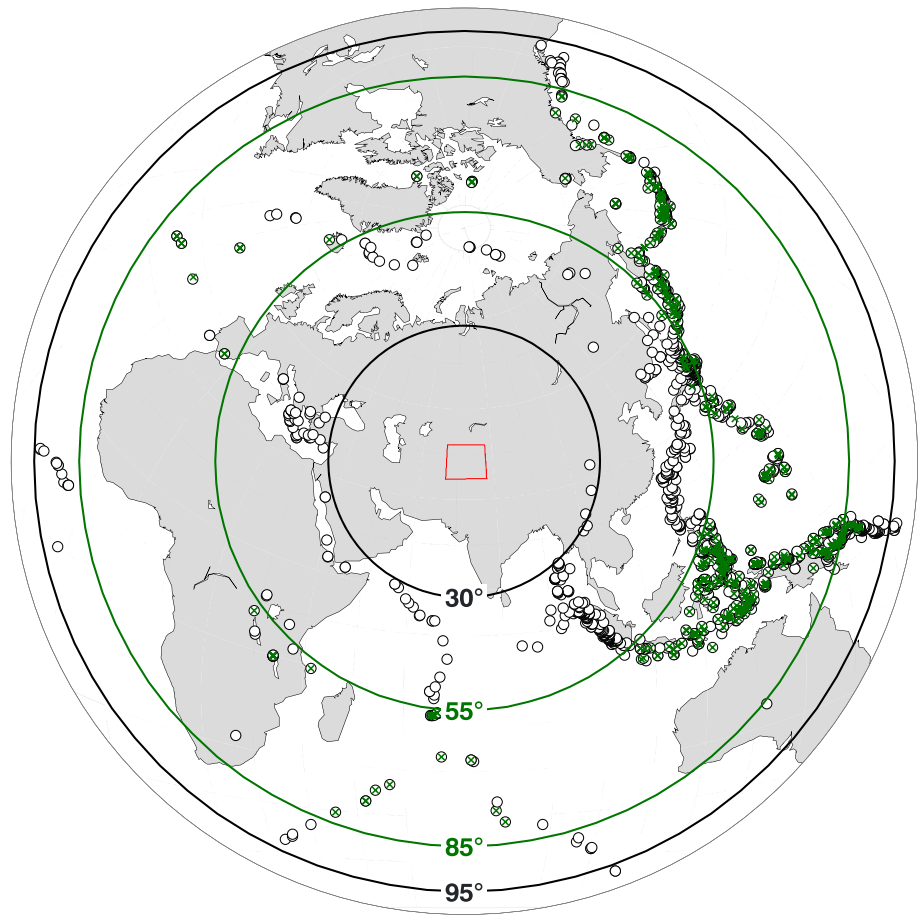


**Figure 2.** Epicenters of teleseismic earthquakes used for  $P$  (1,680 events) and  $S$  wave (540 events) receiver functions (P-RF, circles; S-RF, crosses). The ranges of teleseismic earthquakes used for the P-RF and S-RF methods are 30–95° and 55–85°, respectively. The research area is marked with the red box. Black and green circles show the distances that correspond to the P-RF and S-RF distance ranges, calculated from the center coordinates of the research area (38°N, 72°E).

some permanent stations in Kyrgyzstan, Tajikistan, Afghanistan, and China. Figure 1 shows all stations used in this study (see Kufner et al., 2016; Mechie et al., 2012; Sippl, Schurr, Yuan, et al., 2013 for details). The stations occupy a major portion of the Pamir, southern Tian Shan, Hindu Kush, and parts of the surrounding Tajik, Tarim, and Ferghana Basins.

We applied the  $P$  and  $S$  receiver function (P-RF and S-RF) methods to measure the crustal thickness. The two methods provide independent observations of discontinuities in seismic shear-wave speed (Li et al., 2011). They make use of mode conversions of seismic waves ( $P_s$  or  $S_p$ ) from teleseismic distances at discontinuities such as the Moho. The arrival time of the converted  $P_s$  or  $S_p$  phase is compared to the arrival time of the  $P$  or  $S$  mother phase, respectively, and the converter depth is determined from the time difference between the converted phases and their mother phases. Epicentral distances ranging from 30° to 95° are used for P-RF events. Only a subset of these earthquakes is usable for the S-RF method, for which epicentral distances of 55° to 85° are most suitable (Yuan et al., 2006). Figure 2 shows all events used in our analysis. All records were band-pass filtered (0.5–30 s for P-RFs and 1–30 s for S-RFs). Events with magnitudes larger than 5.5 were inspected and selected manually, with respect to their signal-to-noise ratios. If needed, additional high-pass filters (20, 15, 10, 7.5, or 5 s) were applied to remove low-frequency noise. The three-component records were rotated into the  $L$ - $Q$ - $T$  coordinate system using theoretical back azimuths and incidence angles. For P-RFs, the  $L$  component is deconvolved from the  $Q$  component, and for S-RFs, the  $Q$  component is deconvolved from the  $L$  component. We performed the deconvolution steps using time-domain Wiener filtering with a time window of 100 s.

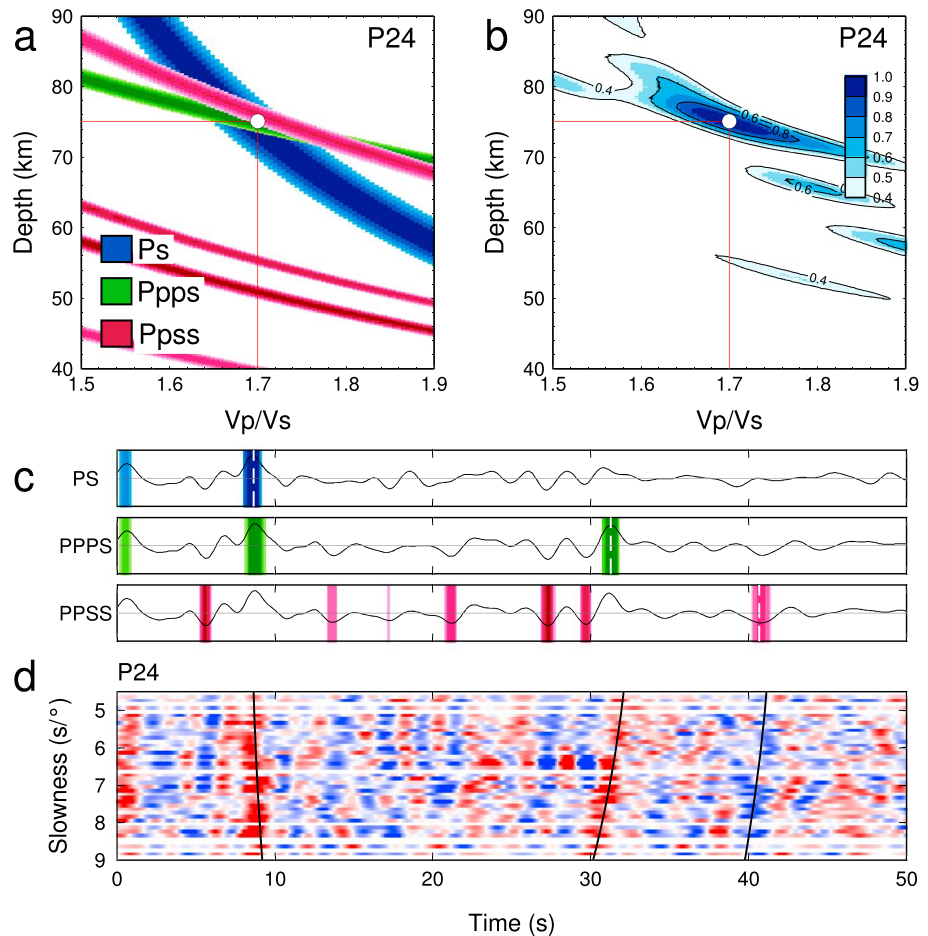


**Figure 3.** Illustration of the extended H- $\kappa$  inspection routine for determination of the Moho depth and average crustal  $V_p/V_s$  ratio from P-RFs of a single station based on 181 events at station P24 in the southeastern Pamir (see Figure 1). (a) Stack contributions of *Ps*, *PpPs*, and *PpSs* phases in a  $V_p/V_s$  depth diagram; only amplitudes of the correct sign above a threshold value are plotted. (b) Stacked *Ps*, *PpPs*, and *PpSs* phases (standard H- $\kappa$  diagram). (c) Summation traces after moveout correction (to a reference slowness of 6.4 s/deg, corresponding to an epicentral distance of 67°) for the direct (*Ps*) and the multiple (*PpPs* and *PpSs*) phases. The color coding corresponds to the color code in Figure 3a. White dashed lines mark the phases selected automatically from the maximum H- $\kappa$  stack (Figure 3b). (d) Individual traces stacked in slowness bins. Positive amplitudes are shown in red, negative in blue; black lines mark the theoretical arrival times of *Ps*, *PpPs*, and *PpSs* phases calculated from the H and  $\kappa$  values with the maximum stacked amplitude (circles in Figures 3a and 3b).

Even though the P- and S-RF methods are in principle similar, they differ in certain aspects. *Ps* phases appear in the coda of the *P* waves, while *Sp* phases arrive earlier than the main *S* phase. P-RFs are often complicated by crustal multiples (*PpPs* and *PpSs* phases). In contrast, *Sp* waves used for S-RFs are precursors of the mother *S* phase and are separated from the multiple reverberations that arrive after the mother phase. However, the crustal multiple phases, which complicate the P-RFs, can also be utilized to determine the crustal average  $V_p/V_s$  ratio. We used the H- $\kappa$  algorithm (Zhu & Kanamori, 2000) for the joint determination of the crustal  $V_p/V_s$  ratio and the crustal thickness from P-RFs. *P* waves contain higher frequencies than *S* waves, therefore allowing for a higher resolution. Moreover, due to the greater suitable distance range, more earthquakes can be used for P-RFs, providing better signal-to-noise ratios.

We used both methods and derived independent measurements for the Moho depth. From the differential arrival times, approximate Moho depths were determined directly by consulting an average one-dimensional velocity model with a constant  $V_p/V_s$  ratio. To get comparable depth results from P-RFs and S-RFs, we applied the  $V_p/V_s$  ratio obtained from the H- $\kappa$  method for the time-depth conversion to

construct both the P-RF and S-RF Moho depths. The results of both methods were combined, so that the uncertainties and errors involved in the individual methods are minimized by averaging.

### 3.1. Determination of Crustal $V_p/V_s$ Ratio and Moho Depth From P-RF

Using the H- $\kappa$  method, the Moho depth and crustal average  $V_p/V_s$  ratio were determined for each station. If shallow crustal converters are present, the multiple phases of these discontinuities can obscure the Moho phase. The H- $\kappa$  algorithm (H stands for the Moho depth and  $\kappa$  for the  $V_p/V_s$  ratio) helps to identify possible candidates of “real”  $P_s$  phases through the association of direct with multiple phases. During the procedure, additional zero-phase low-pass filters were applied in order to suppress signals from intracrustal converters. As default value, a cutoff frequency of 2 s was used. However, at some stations this value was manually tuned in order to optimize the signal-to-noise ratio. Receiver functions are stacked on a H- $\kappa$  grid using the moveout of  $P_s$ ,  $PpPs$ , and  $PpSs$  phases. The maximum stack is regarded as the most likely H- $\kappa$  combination for the Moho phase. To ensure that the H- $\kappa$  stack maximum corresponds to realistic associations between direct and multiple phases, we applied an extended inspection routine. For each station, we examined a combination of different representations of data. Figure 3 visualizes the analysis for station P24, located in the southeastern Pamir (see Figure 1 for station location). While Figure 3b shows the classical representation of the H- $\kappa$  stacking result as introduced by Zhu and Kanamori (2000), the different depth-time relations of the  $P_s$ ,  $PpPs$ , and  $PpSs$  phases can be used separately as shown in Figure 3a. The advantage of the latter data representation is that one can see how many phases join at one H- $\kappa$  combination, which helps to evaluate the reliability of the maximum stack (see Figure 3b). In Figure 3d, the RFs are sorted by their slowness and stacked in bins of 0.1-s/deg slowness intervals. Here the direct and multiple phases can be distinguished from each other by their slopes (moveout). While for direct  $P_s$  phases larger slownesses result in larger arrival times, multiple  $PpPs$  and  $PpSs$  phases show the opposite moveout.

In the three panels of Figure 3c, the summation trace is calculated after moveout corrections for the  $P_s$ ,  $PpPs$ , and  $PpSs$  phases, respectively (Yuan et al., 1997). For the preferred H- $\kappa$  combination based on the stack in Figure 3b, the curves of the theoretical arrival times for the three investigated phases are calculated as a function of slowness. The resulting slowness-arrival time curves are compared with the moveout of the observed data (black lines in Figure 3d). For station P24 (Figure 3), all three phases can be identified clearly. They follow the theoretical moveout curves. We inspected and interpreted these three data representations for each station in order to minimize false associations between the mother phase and the multiples when determining the Moho depth and the  $V_p/V_s$  ratio. The  $V_p/V_s$  values, obtained from the H- $\kappa$  algorithm, are shown in Figure 4 for all stations. The  $V_p/V_s$  values between the stations are interpolated using continuous curvature splines in tension (Smith & Wessel, 1990), implemented in the surface tool of GMT (Wessel & Smith, 1998). H- $\kappa$  analysis was performed for stations where at least one multiple phase is available. If the multiple phases could not be identified clearly, but the  $P_s$  conversion is clear and shows the expected slope in the representation of Figure 3d, only the  $P_s$  time is picked. In those cases (at 17 stations), the crustal thickness was calculated from this  $P_s$  time and a  $V_p/V_s$  value at the station location, deduced from the interpolated  $V_p/V_s$  ratio map (Figure 4).

Figure 5 shows the Moho-depth distribution computed from the P-RFs. At nine stations in the Pamir, we detected two converted phases in the depth range of 60–90 km, providing possible candidates for the Moho. The occurrence of this double Moho phase is discussed in detail (see section 5). Figure 5 shows a map of the Moho depth with the deeper Moho interface chosen; in the inset, the shallower Moho interface has been selected below these nine stations.

### 3.2. Determination of Moho Depth From S-RF and Combination With P-RF

As a complementary observation to the P-RF Moho map, we deduced the crustal thickness from S-RFs. Because the offsets between the conversion points at the Moho from a station are quite large for S-RF (in the order of the Moho depth), they overlap significantly for neighboring stations in our network. Thus, a station-wise analysis would blur the lateral variations. To account for lateral Moho-depth variations and to enhance the converted Moho signals, we computed S-RF cross sections, using common conversion point stacking (Yuan et al., 2000). The Moho depth is then picked from the cross sections.

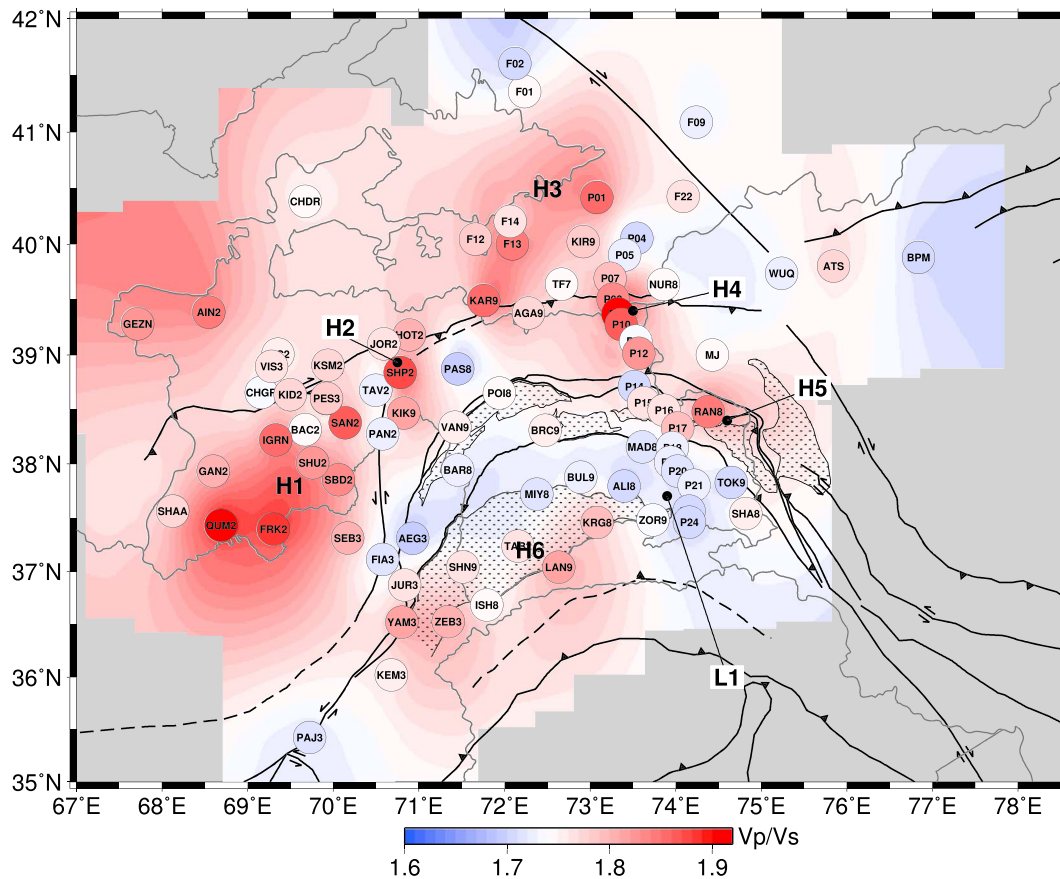


**Figure 4.** Average crustal  $V_p/V_s$  ratio obtained from H- $\kappa$  analysis using  $P_s$ ,  $PpPs$ , and  $PpSs$  arrivals. The ornamented areas mark the locations of the Cenozoic Pamir gneiss domes.  $V_p/V_s$  ratios are interpolated between stations using the procedure of Smith and Wessel (1990) with a tension parameter of  $T = 0.25$ . H1–H6 and L1 mark anomalies of high and low  $V_p/V_s$  ratio, respectively. Grey lines are political boundaries; major faults and suture zones are as in Figure 1.

A series of west-east S-RF cross sections was created in the latitude range between 37° and 40°N for the Moho-depth determination (Figure 6). At each section, we picked the Moho depths at the maximum amplitude approximately every 1°. The time-depth conversion was computed based on a modified IASP91 model (Kennett & Engdahl, 1991) with a crustal thickness of 80 km and a constant  $V_p/V_s$  ratio. To account for local variations of the  $V_p/V_s$  ratio and to allow comparability with the P-RF Moho map, we corrected the S-RF Moho depths using the  $V_p/V_s$  value at the corresponding coordinates from the  $V_p/V_s$  ratio map derived from the H- $\kappa$  analysis (Figure 4). Thus, the Moho depths in Figure 6 are slightly different from the final values. Figure 7 shows the Moho map derived from the S-RFs. Here the values from the cross sections are corrected taking into account the interpolated  $V_p/V_s$  ratios at the positions of the S-RF measurements.

The main features of the S-RF and P-RF Moho maps (Figures 5 and 7) are nearly identical. In Figure S1, we show the differences between the Moho depths derived by the two methods. Since both observations are independent, their similarity corroborates the results. We combined the P-RF and S-RF data sets in one map (Figure 8). For the P-RF Moho depth estimates, we used the station locations as reference points (depicted as triangles in Figure 7). For the S-RFs, the locations of the picks along the cross sections (Figure 6) were used (depicted as squares in Figure 7). The Moho surface was constructed by interpolation through the combined data set in the same way as for the P-RF and S-RF data sets alone.

## 4. Results

### 4.1. Map of Crustal $V_p/V_s$ Ratios

A map of the crustal  $V_p/V_s$  ratios was created by interpolating the individual measurements from the H- $\kappa$  algorithm at each station (Figure 4). Where a double Moho was observed, the  $V_p/V_s$  ratio was determined



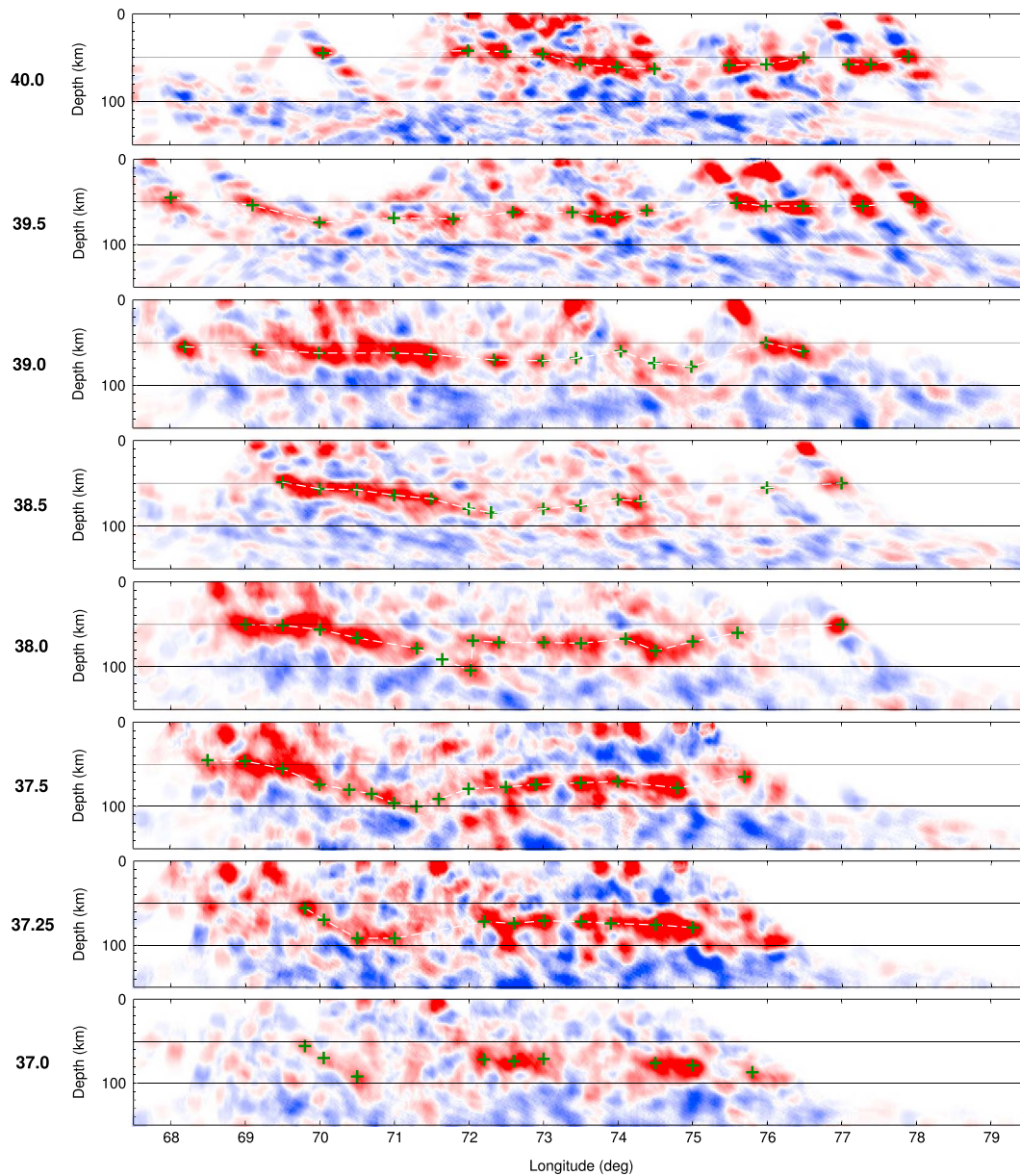


**Figure 6.** West-east S-RF cross sections with picked Moho depths (green crosses). The center latitude ( $^{\circ}$ N) for each cross section is written on the left side for each plot. Amplitudes from converters with a maximum distance of 30 km are projected into each cross section. Red and blue colors denote downward velocity increases and decreases, respectively. A constant  $V_p/V_s$  ratio of 1.73 was applied for the migration. Thus, the final Moho depth values in Figure 7 may differ slightly from the values shown here.

agrees with the results from wide-angle seismic reflections and refractions from local earthquakes along the north-south TIPAGE profile ( $V_p/V_s$  ratio of 1.77 beneath the North Pamir, and 1.69 beneath the South and Central Pamir; Mechie et al., 2012).

#### 4.2. Crustal Thickness Map

We created a map of crustal thickness by combining P-RF and S-RF measurements (Figure 8). Over the entire study area, the crustal thickness varies significantly, from 35 to 55 km below the basins to a double normal thickness of 65–75 km in the Pamir and Hindu Kush. It locally reaches ~90 km in the western Central Pamir. Note that an inclined Moho interface would yield an underestimated Moho depth as H- $\kappa$  result as we found from synthetic tests (see Figure S2 in the supporting information). In the

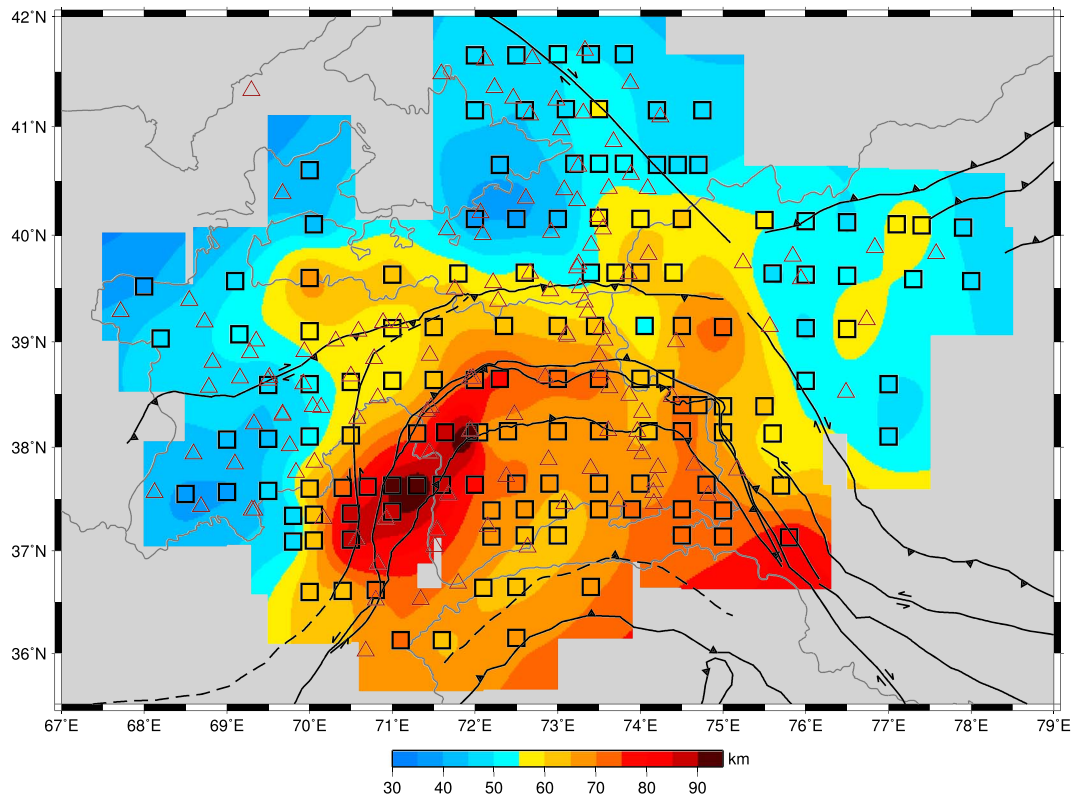


**Figure 7.** Moho map from S-RF picks. Squares show the locations of picked S-RF Moho depths and triangles the locations of the seismic stations. Values for the Moho depth are derived from Figure 6 and corrected taking into account the corresponding  $V_p/V_s$  values shown in Figure 4. For interpolation between all single measurements, we used the interpolation procedure of Smith and Wessel (1990) with a tension parameter of  $T = 0.25$ .

central part of the Tajik Basin, the crustal thickness is 35–45 km and increases to ~55 km toward the Pamir. This result is in general agreement with the crustal thickness derived by controlled-source, wide-angle profiles (Kulagina et al., 1974 discussed in Burtman & Molnar, 1993). Our data sampled the southern and western parts of the Ferghana Basin, where the crustal thickness is 40–45 km beneath the sedimentary basin; it increases to ~50 km beneath the Talas-Ferghana Fault. In the Tarim Basin, the crust is ~50 km thick, ~5 km thicker than that of the Tajik and Ferghana Basins. Although our data only cover the western edge of the Tarim Basin, the estimates are consistent with the 45–50-km crustal thickness revealed by controlled-source seismic data in the central Tarim Basin (Li et al., 2006).

The orogenic areas are underlain by thick crust. The southwestern Tian Shan stands out in Figure 8 as an east-west trending feature with 55–65-km-thick crust. The crustal thickness of the Hindu Kush increases slightly toward the southern Pamir from ~60 to 65 km. The crust in the Pamir is overall thicker than ~65 km and exhibits significant lateral variations, which do not follow the geological division into the North, Central, and South Pamir. The North Pamir has an ~65-km-thick crust. At nine stations, mainly located in the western Central Pamir between the Darvaz Fault/Tanymas Suture and the Rushan-Pshart Zone, we detected two discontinuities at depths of roughly 60–70 and 80–95 km, respectively; both are candidates for the Moho (see also H- $\kappa$  results of three example stations located in the double Moho zone in Figures S3–S5 in the supporting information). In the following, we call this double Moho structure the Moho doublet. The main Moho map in Figure 8 is based on the deeper discontinuity at these nine stations, while in the inset, the shallower discontinuity defines the Moho map. To the east and southeast, the crust thins to 50–60 km in the eastern Central Pamir and to ~65 km in the central South Pamir; it thickens to 75 km in the eastern South Pamir along the transition to Tibet, that is, into the narrowest part of the entire orogen.

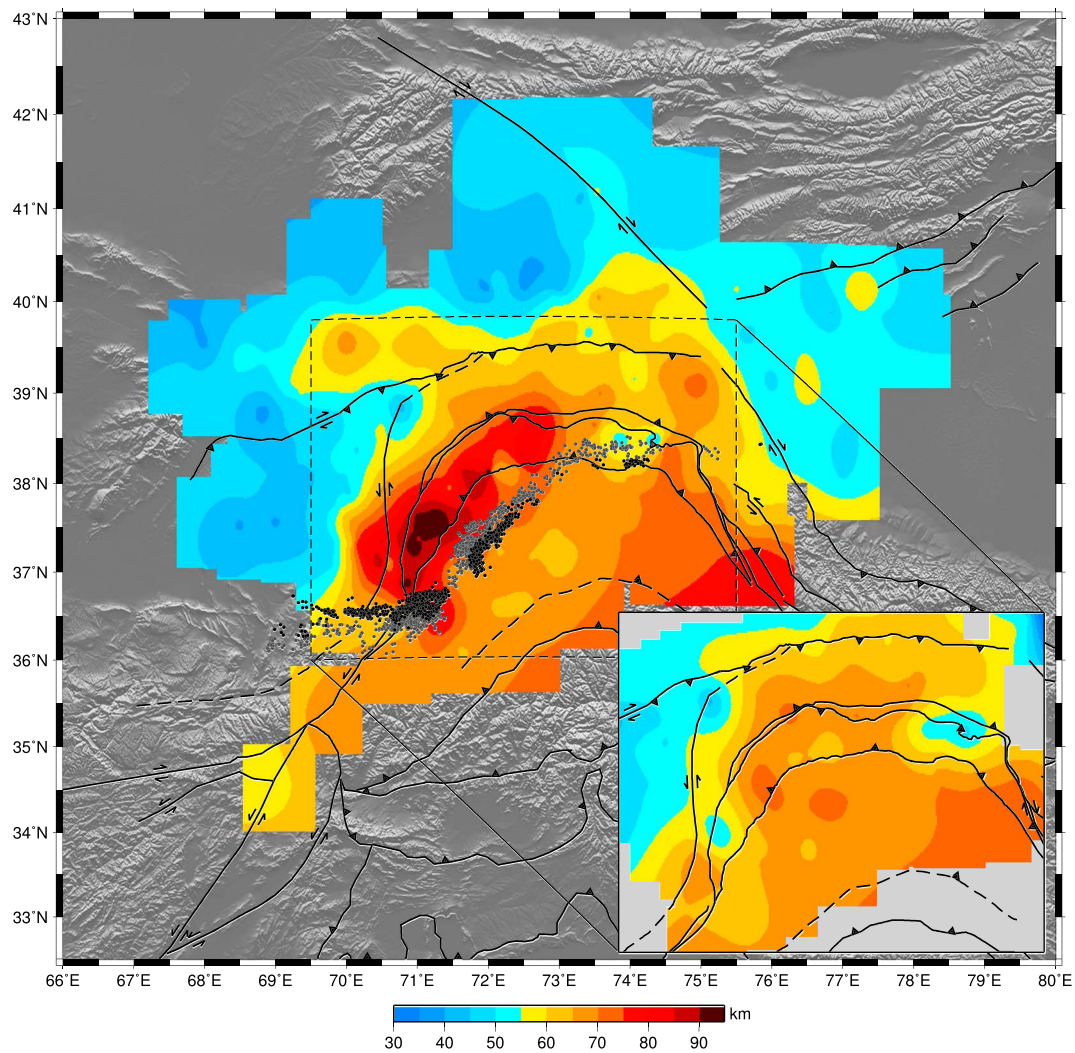


**Figure 8.** Moho map combining P-RF (deep Moho phase in Figure 5) and S-RF observations. At nine stations in the western and northwestern Pamir, where the Moho depth exceeds 80 km, two Moho phases were detected from P-RFs (see Figure 5). In the main figure, the deeper Moho interface, which is continuous to the east and northeast, was chosen. The inset shows the Moho map with the shallower Moho, which is continuous to the west and southwest, selected at those nine stations (see also Figures 9 and 10).

## 5. Discussion

### 5.1. Crustal Underthrusting and Delamination Beneath the Pamir

In most areas of the Pamir, the crust is twice as thick as the global continental average (~35 km; e.g., Hacker et al., 2015; Kennett & Engdahl, 1991), similar to Tibet. The thickest crust is observed along a southwest-northeast trending trough between the Darvaz fault/Tanymas suture and the Rushan-Pshart Zone, mostly in the western Central Pamir region. Here the crust is up to 90 km thick, making it, to our knowledge, nominally the thickest on Earth. At several stations in this region, we detected Moho doublets by P-RF. The Moho trough and doublet zone is parallel to the boundary region of the Pamir to the Tajik Basin and runs parallel to the intermediate-depth seismic zone on its northwestern side (Figure 8). We interpret the extremely thick crust and the Moho doublet as evidence for crustal stacking of the converging tectonic units beneath the Pamir. We cannot exclude the presence of a thin mantle wedge below the shallower Moho. The thick, mostly Gondwana-derived Pamir crust thrusts over the cratonic Asian lithosphere, that is, the lithosphere of the Tajik Basin. At greater depths, in the upper mantle, the cratonic Asian crust is detached from the overlying Pamir crust, leaving a mantle wedge between the upper and lower plates. The deeper Moho interface continues to the south and southeast as a dipping interface, following

the intermediate-depth seismicity. This interface has been resolved along the TIPAGE seismic profile in the eastern Central Pamir. Schneider et al. (2013) identified a second interface with negative velocity contrast on top of the lower plate, outlining a low-velocity zone with a thickness of 10–15 km down to a depth of >150 km. Sippl, Schurr, Tynpel, et al. (2013) observed a low-velocity anomaly by local earthquake tomography and interpreted it as deeply buried middle crustal material which has been pulled to depth by the delaminating and retreating cratonic Asian lithospheric mantle. The interpretation of the continental nature of the crust is plausible, since there is no geological evidence for the presence of oceanic crust in the area of the Pamir, and the low-velocity zone connects to the Tajik Basin crust, where the Moho is observed at 40–50-km depth, dipping toward the Pamir.

An example for the Moho doublet observation at station BRC9 is shown in Figures 9a–9c. In the H- $\kappa$  analysis (Figures 9a and 9b), two maxima occur at ~65- and 88-km depth with  $V_p/V_s$  ratios of 1.72 and 1.75, respectively. Figure 9c shows a southeast-northwest P-RF cross section, perpendicular to the strike of the seismic zone (B-B'; see Figure 5 for profile location). In this cross section, the deeper (Asian) Moho continues toward the northwest, while the shallow (Pamir) Moho continues toward the southeast. Beneath the western and central South Pamir, the Asian crust has detached from a 60–70-km-thick Pamir crust. The Pamir crust thins locally to ~50 km beneath the eastern Central Pamir around stations RAN8 and P16 (Figures 9d–9h), thinner than beneath the rest of the Pamir (Figure 8). The H- $\kappa$  analysis for both stations shows a clear maximum at the attributed Moho depth (Figures 9d–9g). For station P16, the  $P_s$  and  $PpPs$  are unambiguously detectable. At station RAN8, where the Moho depth is at its minimum, both multiple reverberations ( $PpPs$  and  $PpSs$ ) confirm the depth of the direct  $P_s$  phase. Along profile A-A' (location shown in Figure 5), strong variations in the Moho depth can be seen in this region between 38 and 39°N (Figure 9h). The Moho shallows from 39 to 38.5°N and deepens again to 38°N. Strong crustal deformation has been inferred in this region from seismic anisotropy (Kufner, Eken, et al., 2018). The thinning of the Pamir crust at 38.5°N can be explained by the buckling effect due to the delamination and rollback of the cratonic Asian lithosphere beneath the thick crust and lithosphere of the Pamir. Along both profiles (Figures 9c and 9h), the shallower Moho is the base of the Pamir crust that thrusts over the delaminating and retreating cratonic Asian lithosphere of the Tajik-Tarim Basins, marked by the deeper Moho (Schneider et al., 2013). The Pamir Moho indicates that the underlying mantle wedge locally extends upward to a depth as shallow as ~50 km on top of the delaminating Asian crust and lithosphere. The locations of the shallow Moho detections along profiles A-A' and B-B' coincide with the position of the Muskol-Shatput and the Sarez domes at the surface, respectively (Figure 1).

Double Moho structures have also been observed in southern Tibet beneath the Lhasa terrane and were interpreted as a result of the underthrusting of the Indian lower crust beneath the Tibetan crust (Kind et al., 2002; Nábělek et al., 2009; Xu et al., 2017). These observations revealed that the northern front of the underthrusting Indian crust does not extend north beyond the Lhasa terrane and is apparently detached from the underlying Indian mantle lithosphere. In contrast to Tibet, no evidence was found for Indian crust beneath the Pamir. Instead, cratonic Asian crust underlies the North Pamir and has detached beneath the Central and South Pamir to a depth of at least 150 km, hosting the intermediate-depth seismicity (Figure 10).

## 5.2. Felsic Composition of the Pamir Crust

The  $V_p/V_s$  ratios determined in this study are a crustal average below each station from the surface to the Moho, implying that much larger variations are possible within single layers.  $V_p/V_s$  ratios largely depend on the rock physical properties and composition (Christensen, 1996), with only a weak dependence on pressure and temperature. Generally, felsic rocks have a low  $V_p/V_s$  ratio, while mafic rocks have a high  $V_p/V_s$  ratio. Quartz is the most important crustal constituent reducing the  $V_p/V_s$  ratio; the  $V_p/V_s$  ratio of a single quartz crystal in the  $\alpha$  state can be as low as 1.5 (Christensen, 1996). The presence of fluid or local melt reduces the shear wave velocity more dramatically than the compressional wave velocity, thus increasing the  $V_p/V_s$  ratio. Continental crust has average  $V_p/V_s$  ratios of 1.75–1.77 (e.g., Christensen, 1996; Zandt & Ammon, 1995), and is usually composed of felsic upper crust with lower  $V_p/V_s$  ratios (roughly <1.75) and mafic lower crust with higher  $V_p/V_s$  ratios (roughly >1.75).

Our analysis revealed low crustal  $V_p/V_s$  ratios (~1.70) in much of the Central and South Pamir, indicating that the crust is felsic, rich in  $\alpha$ -quartz in the upper crust (Figure 4). In the regions of the gneiss domes,

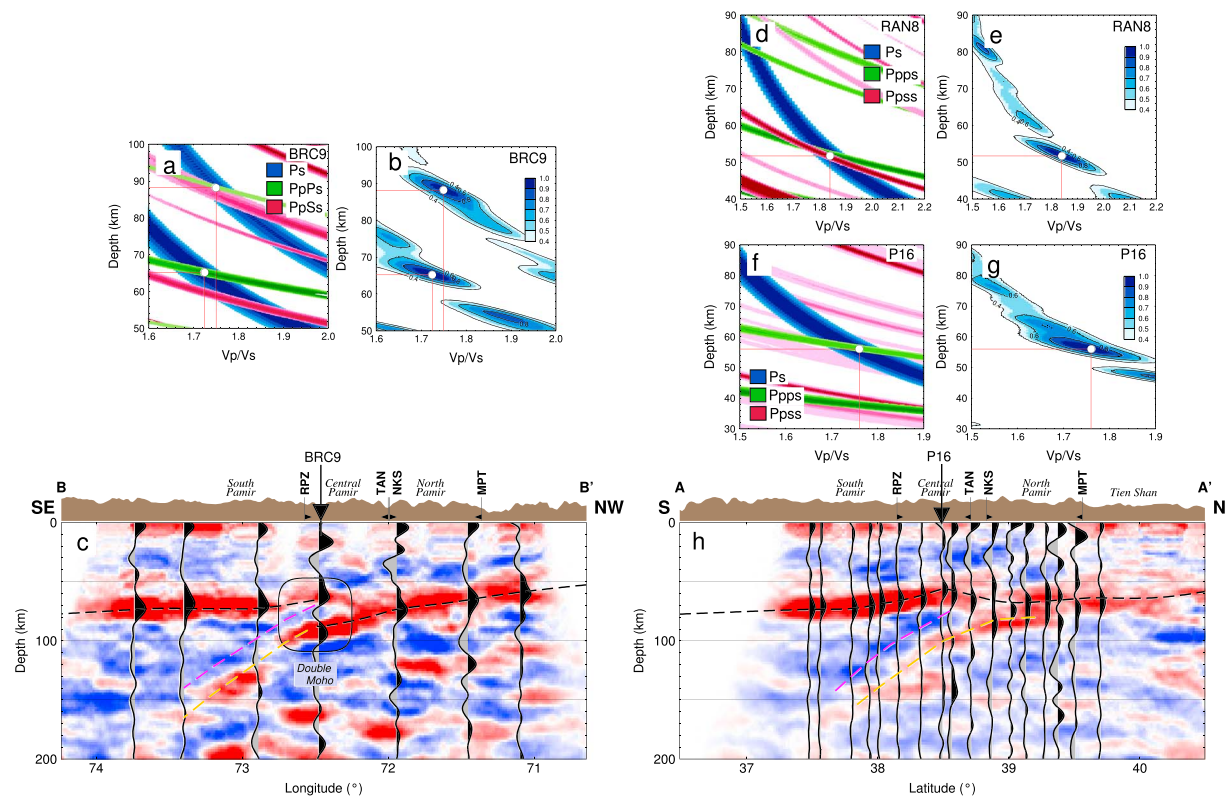


**Figure 9.** Examples of Pamir stations with a thick crust, a double Moho, and a shallow Moho. (a–c) P-RF data showing the double Moho phase at the location of the Moho trough. (a and b) H- $\kappa$  analysis for station BRC9 showing two maxima in the  $V_p/V_s$ -depth diagrams. (c) Migrated northwest-southeast cross section passing through BRC9. The black dashed lines mark the interpolated Moho depths. Orange and magenta dashed lines mark the lower and upper interface of the Asian slab's lower crust. While to the northwest of BRC9 the deeper Moho is plotted in Figure 8, the shallower Moho is plotted to the southeast of BRC9. Location of the cross-section line B-B' is shown in Figure 5. (d–h) P-RF data showing the shallow Moho anomaly in the eastern Central Pamir. (d–g) H- $\kappa$  analysis for stations P16 and RAN8, showing a Moho depth of ~56 and 52 km, respectively. (h) P-RF north-south cross section passing through station P16. Line A-A' is shown in Figure 5. The moveout corrected summation trace of each station is converted to depth, normalized to the Moho amplitude, and plotted vertically as black wiggles on top of the migrated data. Surface topography and tectonic units are shown at the top. Station RAN8 (not shown), which has the thinnest crust in the Pamir, is situated in this projection at the same location as P16. In the cross sections, a constant  $V_p/V_s$  ratio of 1.73 was assumed, and depths are shown relative to the surface (not sea level). The summation trace of the Moho phase at station P16 shows its maximum at ~57-km depth. The increased  $V_p/V_s$  ratios at stations P16 and RAN8 reduce the Moho depth to ~50 km.

the  $V_p/V_s$  ratios are slightly to significantly elevated (1.76 to 1.84), which can be explained by the presence of layers within the crust with a very high  $V_p/V_s$  ratio modifying the crustal average. A candidate layer with high  $V_p/V_s$  ratio is the low-velocity layer observed at depths of 15–40 km beneath the South Pamir (Li et al., 2018; Sippl, Schurr, Tymphel, et al., 2013). Assuming a 20-km-thick midcrustal layer with a  $V_p/V_s$  ratio of 2.00 in a 70-km-thick crust with a  $V_p/V_s$  ratio of 1.69, an average crustal  $V_p/V_s$  ratio of 1.78 is inferred. Such a high  $V_p/V_s$  ratio (2.00) within the crust could indicate a zone containing partially molten rocks (e.g., H5 and H6; Figure 4). Comparable  $V_p/V_s$  ratios have also been observed in Tibet (e.g., review in Mechie & Kind, 2013).

In the South and Central Pamir, areas of elevated  $V_p/V_s$  ratios coincide with the Shakh dara (H6) and the Muskol-Shatput (H5) gneiss domes (ornamented areas in Figure 4). The slightly elevated  $V_p/V_s$  values at stations VAN9 and POI8 overlap with the Yazgulom gneiss dome. These high-grade gneiss domes formed by large-scale crustal extension with exhumation from 30–50-km depth (Hacker et al., 2017; Rutte, Ratschbacher, Schneider, et al., 2017; Rutte, Ratschbacher, Khan, et al., 2017; Stübner, Ratschbacher, Rutte, et al., 2013; Stübner, Ratschbacher, Weise, et al., 2013), exposing felsic crustal rocks (see section 2). Migmatites, formed by partial melting of metapelites, are widespread in the Shakh dara dome, but are rare in the other domes. Felsic granitoids are common in all domes. From thermochronologic studies, Stübner, Ratschbacher, Weise, et al. (2013) inferred syn-exhumation geothermal gradients of ~60 °C/km for the

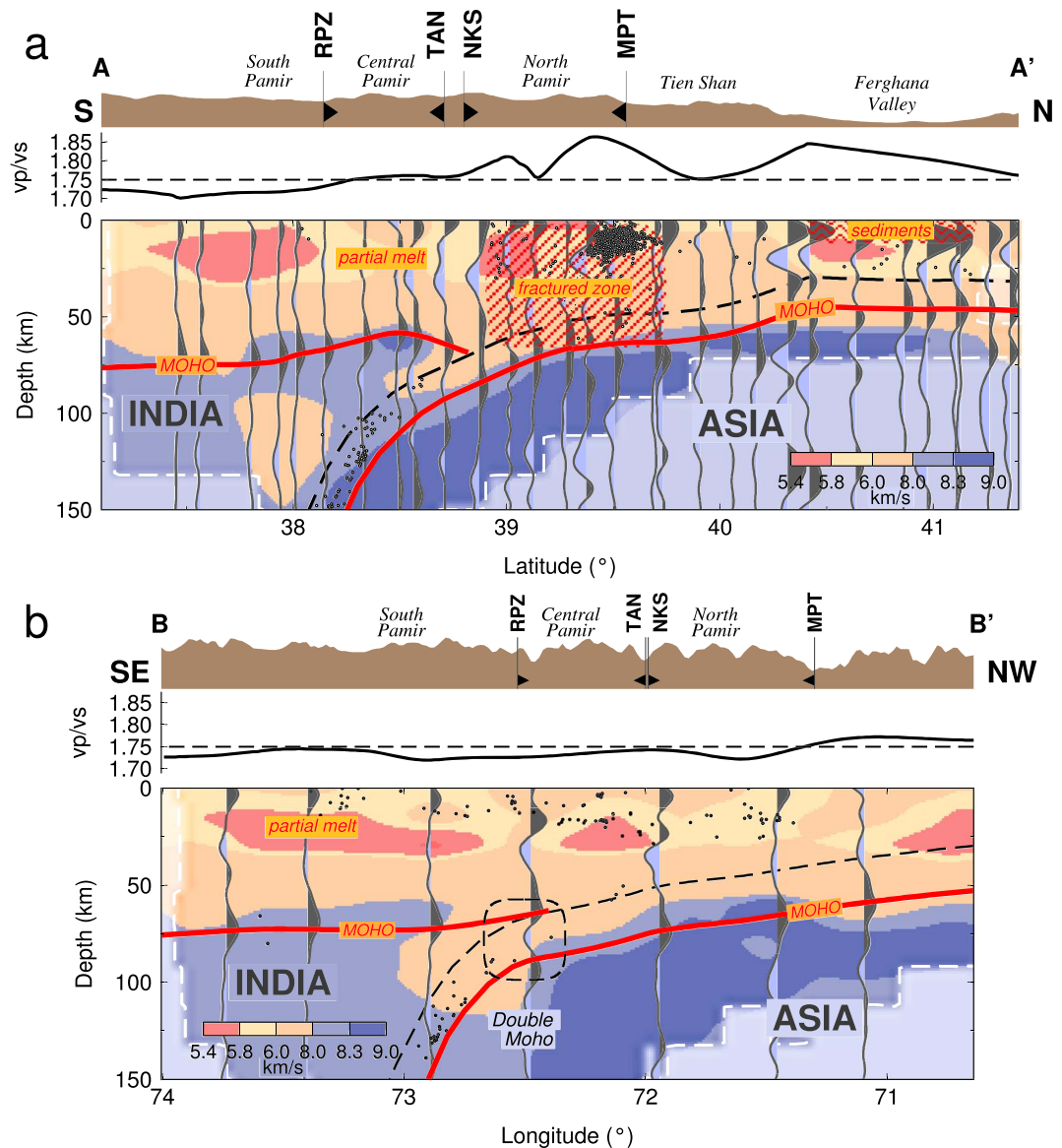


**Figure 10.** Present-day configuration of the Pamir crust along cross sections (a) A-A' and (b) B-B'. The average crustal  $V_p/V_s$  ratio is low ( $<1.7$ ) in the South Pamir, since the mafic lower crust is missing. Interpretations for increased  $V_p/V_s$  ratios are marked: a partial melt layer in the Central and South Pamir that coincides with the location of the domes, fracturing and fluids around the Main Pamir Thrust, and thick sediments in the Ferghana Basin increase the average crustal  $V_p/V_s$  ratio. Small black dots represent earthquakes. Background colors show the  $P$  wave velocity model of Sippl, Schurr, Tympel, et al. (2013) where badly resolved areas (outside the white dashed lines) have been faded.

Shakhdara dome, which relaxed toward the end of exhumation at 4–2 Ma. At present, a still high geothermal gradient of  $\sim 40$  °C/km was estimated, confirmed by the occurrence of numerous hot springs in the region. A geothermal gradient of 40 °C/km would imply temperatures  $>700$  °C below  $\sim 18$  km, exceeding the melting temperature of the metapelites. Nearly all the samples analyzed by Hacker et al. (2017) from the Shakhdara dome show temperatures exceeding the metapelite solidus at  $\sim 20$ –15 Ma. Duchkov et al. (2001) reported high heat-flow values of  $120$  mW/m<sup>2</sup> in the South Pamir, consistent with the high temperatures in the crust. Furthermore, local earthquake tomography revealed low  $V_p$  values (5.6–5.7 km/s) in the depth range from 15 to 30 km (Sippl, Schurr, Tympel, et al., 2013), indicating that  $V_s$  must be decreased even more strongly to match the observed high  $V_p/V_s$  ratio. Surface wave tomography (Li et al., 2018) also imaged a low  $V_s$  anomaly in the middle crust at depths of 20–40 km below the Shakhdara dome. Thus,

the observation of low  $V_p$  and a high  $V_p/V_s$  ratio might be best explained by the presence of partially molten rocks. This interpretation is in agreement with results of the magnetotelluric survey by Sass et al. (2014), who observed high electrical conductivity below the South Pamir at a depth of 10–15 km.

We propose that the low bulk crustal  $V_p/V_s$  ratio beneath the Central and South Pamir outside the domes (L1 in Figure 4) resulted from the loss of the mafic Pamir lower crust by lithospheric delamination/foundering. Low  $V_p/V_s$  ratios were also observed in the crust beneath other orogenic belts, such as beneath Tibet (e.g., Tian & Zhang, 2013) and the central Andes (Beck et al., 1996). Delamination of mafic lower crust due to gravitational instability may occur in collisional orogens when the crust is overthickened. This delamination process changes the bulk composition of the continental crust. With the increase of crustal thickness, the mafic lower crust is subject to eclogitization and becomes denser. At a certain point, the eclogitized rocks detach from the felsic crust and founder into the mantle. The remaining felsic upper and middle crust continues to thicken during the convergence and finally constitutes the present-day crust, characterized by a low  $V_p/V_s$  ratio. An additional contribution to the thick Pamir crust may come from relamination of the felsic component of the delaminated lithosphere in the uppermost mantle after its chemical differentiation (Hacker et al., 2015).

By analyzing xenoliths erupted in the southeastern Pamir, Kooijman et al. (2017) and Shaffer et al. (2017) reconstructed an evolution of crustal foundering from ~20 to 11 Ma (see section 2). The xenoliths, with a continental-crust composition, indicate the recycling of the Gondwana-derived continental crust of the South Pamir into the mantle (Gordon et al., 2012; Hacker et al., 2005). The crustal foundering occurred when the advancing cratonic Indian lithosphere approached the cratonic Asian (Tajik-Tarim Basin) lithosphere at ~14 Ma and terminated at ~11 Ma when the two plates finally made contact and the xenoliths were ejected to the surface (Shaffer et al., 2017). The progressive indentation of the Indian lithosphere below the Pamir has been proposed to have caused the rollback of the Asian lithosphere and progressed until the picture seen today (Kufner et al., 2016; Schneider et al., 2013; Sippl, Schurr, Tympel, et al., 2013; this study). In Figure 10, we summarize our interpretation and compare our results to the local earthquake tomography of Sippl, Schurr, Tympel, et al. (2013). During plate convergence, the South and Central Pamir crust lost the overthickened mafic lower crustal root by crustal delamination and regained a felsic root by continuous thickening and—possibly—by relamination. Overall, the tomography fits well to the results inferred from the receiver functions. In Figure 10b, the locations of partial melt in the upper crust interpreted from  $V_p/V_s$  observations coincide with regions of low  $P$  wave speed (<5.8 km/s). In Figure 10a, however, a lateral offset of the low  $P$  wave -speed anomaly and the dome position is present, which can be explained by a smearing effect of the tomographic inversion, since the low-velocity anomaly of the Shakh dara dome is located west of the profile, which might be projected onto the profile beneath South Pamir.

Besides the presence of partial melt, the  $V_p/V_s$  ratio is also modified by fracturing and the presence of fluids in the vicinity of fault zones. The observed increased  $V_p/V_s$  in the North Pamir (H4; Figure 4) south of the Main Pamir Thrust and southeast of the Garm region (H2; Figure 4), where the shallow seismic activity is focused (Kufner, Schurr, et al., 2018; Schurr et al., 2014) and released in periodically occurring large earthquakes (e.g., the 2008  $M_w$  6.6 Nura event; Sippl et al., 2014), is attributed to strong fracturing. North of the Main Pamir Thrust and west of the Darvaz Fault,  $V_p/V_s$  is generally high in the Ferghana Basin (H3) and the Tajik Basin (H1), presumably due to very high  $V_p/V_s$  ratios of the sedimentary layers and possibly also due to the mafic lithology in the crystalline basement of the Basins (Sippl, Schurr, Tympel, et al., 2013).

## 6. Conclusions

We constructed maps of the crustal thickness and the  $V_p/V_s$  ratio of the Pamir and surrounding regions by a combination of  $P$  and  $S$  receiver functions using teleseismic waveform data recorded by temporary and permanent seismic stations. The crustal thickness varies from 35 to 50 km beneath the Tajik, Tarim, and Ferghana Basins to over 70 km in the Pamir and Hindu Kush and it reaches up to 65 km in parts of the Tian Shan. Beneath the Central Pamir, a double Moho structure is the result of the westward and northward delamination and rollback of the cratonic Asian lower crust of the Tajik-Tarim Basins beneath the Pamir. Much of the South and Central Pamir crust is characterized by low  $V_p/V_s$  ratios, suggesting a felsic bulk composition. This is explained by the loss of mafic rocks due to crustal delamination/foundering during the continuous plate convergence. The moderate to high  $V_p/V_s$  ratios beneath the Central and South

Pamir gneiss domes may be caused by the existence of zones of partially molten rocks. The highest  $V_p/V_s$  values outside the sedimentary basins are found south of the Main Pamir Thrust, where they likely indicate the presence of a fractured water-bearing damage zone.

#### Acknowledgments

The TIPAGE project was funded by the Deutsches GeoForschungsZentrum GFZ and the Deutsche Forschungsgemeinschaft (DFG Bundle 443). The TIPTIMON project was funded by the German Federal Ministry of Education and Research (support code 03G0809) within the CAME program. The GFZ additionally financed the station deployments of the three networks. Seismic stations were provided by the Geophysical Instrument Pool of the GFZ. Waveform data of temporary experiments are archived at the GEOFON data center (FDSN codes: TIPAGE: 7B 2008–2010; FERGHANA: 6C 2009–2010 and 2013–2014, TASK FORCE KIRGISTAN: 4B 2008–2009; TIPTIMON TJ: 5C 2012–2014, TIPTIMON AF: 6C 2013–2014). Data can be obtained via the GEOFON Data Management Center (<https://geofon.gfz-potsdam.de/waveform/archive>). Waveform data of the permanent stations were provided by the GEOFON, IRIS, and the Chinese Earthquake Network Center. We are grateful to all team members of the field experiments. We used Seismic Handler (Stammler, 1993) for the receiver function processing and GMT (Wessel & Smith, 1998) for the production of most figures.

#### References

- Angiolini, L., Zanchi, A., Zanchetta, S., Nicora, A., & Vezzoli, G. (2013). The Cimmerian geopuzzle: New data from south Pamir. *Terra Nova*, 25(5), 352–360. <https://doi.org/10.1111/ter.12042>
- Beck, S. L., Zandt, G., Myers, S. C., Wallace, T. C., Silver, P. G., & Drake, L. (1996). Crustal thickness variations in the central Andes. *Geology*, 24(5), 407–410. [https://doi.org/10.1130/0091-7613\(1996\)024<0407:CTVITC>2.3.CO;2](https://doi.org/10.1130/0091-7613(1996)024<0407:CTVITC>2.3.CO;2)
- Belousov, V. V., Belyaevsky, N. A., Borisov, A. A., Volvovsky, B. S., Volkovsky, I. S., Resvoy, D. P., et al. (1980). Structure of the lithosphere along the deep seismic sounding profile: Tien Shan-Pamirs-Karakorum-Himalayas. *Tectonophysics*, 70(3–4), 193–221. [https://doi.org/10.1016/0040-1951\(80\)90279-6](https://doi.org/10.1016/0040-1951(80)90279-6)
- Billington, S., Isacks, B. L., & Barazangi, M. (1977). Spatial distribution and focal mechanisms of mantle earthquakes in the Hindu Kush-Pamir region: A contorted Benioff zone. *Geology*, 5(11), 699–704. [https://doi.org/10.1130/0091-7613\(1977\)5%3C699:SDAFMO%3E2.0.CO;2](https://doi.org/10.1130/0091-7613(1977)5%3C699:SDAFMO%3E2.0.CO;2)
- Burtman, V. S., & Molnar, P. (1993). Geological and geophysical evidence for deep subduction of continental crust beneath the Pamir. *Special Papers - Geological Society of America*, 281, 1–76. <https://doi.org/10.1130/SPE281-p1>
- Chapman, J. B., Scoggin, S. H., Kapp, P., Carrapa, B., Ducea, M. N., Worthington, J., et al. (2018). Mesozoic to Cenozoic magmatic history of the Pamir. *Earth and Planetary Science Letters*, 482, 181–192. <https://doi.org/10.1016/j.epsl.2107.10.041>
- Chatelain, J. L., Roecker, S. W., Hatzfeld, D., & Molnar, P. (1980). Microearthquake seismicity and fault plane solutions in the Hindu Kush Region and their tectonic implications. *Journal of Geophysical Research*, 85(B3), 1365–1387. <https://doi.org/10.1029/JB085iB03p01365>
- Christensen, N. I. (1996). Poisson's ratio and crustal seismology. *Journal of Geophysical Research*, 101(B2), 3139–3156. <https://doi.org/10.1029/95JB03446>
- Cowgill, E. (2010). Cenozoic right-slip faulting along the eastern margin of the Pamir salient, northwestern China. *Geological Society of America Bulletin*, 122(1–2), 145–161. <https://doi.org/10.1130/B26520.1>
- Duchkov, A. D., Shvartsman, Y. G., & Sokolova, L. S. (2001). Deep heat flow in the Tien Shan: Advances and drawbacks. *Geologiya i Geofizika*, 42(10), 1516–1531.
- Fan, G., Ni, J. F., & Wallace, T. C. (1994). Active tectonics of the Pamirs and Karakorum. *Journal of Geophysical Research*, 99(B4), 7131–7160. <https://doi.org/10.1029/93JB02970>
- Gordon, S. M., Luffi, P. I., Hacker, B. R., Valley, J. W., Spicuzza, M., Kozdon, R., et al. (2012). The thermal structure of continental crust in active orogens: Insight from Miocene eclogite- and granulite-facies xenoliths of the Pamir. *Journal of Metamorphic Geology*, 30(4), 413–434. <https://doi.org/10.1111/j.1525-1314.2012.00973.x>
- Grew, E. S., Pertsev, N. N., Yates, M. G., Christy, A. G., Marquez, N., & Chernosky, J. C. (1994). Sapphirine + forsterite and sapphirine + humite group minerals in an ultra-magnesian lens from Kuhl-lal, SW Pamirs, Tajikistan: Are these assemblages forbidden? *Journal of Petrology*, 35(5), 1275–1293. <https://doi.org/10.1093/petrology/35.5.1275>
- Haberland, C., Abdybachev, U., Schurr, B., Wetzel, H.-U., Roessner, S., Sarnagoev, A., et al. (2011). Landslides in southern Kyrgyzstan: Understanding tectonic controls. *Eos, Transactions American Geophysical Union*, 92, 169. <https://doi.org/10.1029/2011EO20001>
- Hacker, B. R., Kelemen, P. B., & Behn, M. D. (2015). Continental lower crust. *Annual Review of Earth and Planetary Sciences*, 43(1), 167–205. <https://doi.org/10.1146/annurev-earth-050212-124117>
- Hacker, B. R., Luffi, P., Lutkov, V., Minaev, V., Ratschbacher, L., Plank, T., et al. (2005). Near-ultrahigh pressure processing of continental crust: Miocene crustal xenoliths from the Pamir. *Journal of Petrology*, 46(8), 1661–1687. <https://doi.org/10.1093/petrology/egi030>
- Hacker, B. R., Ratschbacher, L., Rutte, D., Stearns, M. A., Malz, N., Stübner, K., et al. (2017). Building the Pamir Tibet Plateau: Crustal stacking, extensional collapse, and lateral extrusion in the Pamir: 3. Thermobarometry and petrochronology of deep Asian crust. *Tectonics*, 36, 1743–1766. <https://doi.org/10.1002/2017TC004488>
- Kennett, B. L. N., & Engdahl, E. R. (1991). Travel times for global earthquake location and phase identification. *Geophysical Journal International*, 105(2), 429–465. <https://doi.org/10.1111/j.1365-246X.1991.tb06724.x>
- Kind, R., Yuan, X., Saul, J., Nelson, D., Sobolev, S. V., Mechie, J., et al. (2002). Seismic images of crust and upper mantle beneath Tibet: Evidence for Eurasian plate subduction. *Science*, 298(5596), 1219–1221. <https://doi.org/10.1126/science.1078115>
- Kooijman, E., Smit, M. A., Ratschbacher, L., & Kylander-Clark, A. R. C. (2017). A view into crustal evolution at mantle depths. *Earth and Planetary Science Letters*, 465, 59–69. <https://doi.org/10.1016/j.epsl.2017.02.032>
- Koulakov, I. (2011). High frequency  $P$  and  $S$  velocity anomalies in the upper mantle beneath Asia from inversion of worldwide traveltimes data. *Journal of Geophysical Research*, 116, B04301. <https://doi.org/10.1029/2010JB007938>
- Kufner, S.-K., Eken, T., Tilmann, F., Schurr, B., Yuan, X., Mechie, J., et al. (2018). Seismic anisotropy beneath the Pamir and the Hindu Kush: Evidence for contributions from crust, mantle lithosphere, and asthenosphere. *Journal of Geophysical Research: Solid Earth*, 123, 10,727–10,748. <https://doi.org/10.1029/2018JB015926>
- Kufner, S.-K., Schurr, B., Haberland, C., Zhang, Y., Saul, J., Ischuk, A., & Oimahmadov, I. (2017). Zooming into the Hindu Kush slab break-off: A rare glimpse on the terminal stage of subduction. *Earth and Planetary Science Letters*, 461, 127–140. <https://doi.org/10.1016/j.epsl.2016.12.043>
- Kufner, S.-K., Schurr, B., Ratschbacher, L., Murodkulov, S., Abdulhameed, S., Ischuk, A., et al. (2018). Seismotectonics of the Tajik basin and surrounding mountain ranges. *Tectonics*, 37, 2404–2424. <https://doi.org/10.1029/2017TC004812>
- Kufner, S.-K., Schurr, B., Sippl, C., Yuan, X., Ratschbacher, L., Akbar, A. S. o M., et al. (2016). Deep India meets deep Asia: Lithospheric indentation, delamination and break-off under Pamir and Hindu Kush (central Asia). *Earth and Planetary Science Letters*, 435, 171–184. <https://doi.org/10.1016/j.epsl.2015.11.046>
- Kulagina, M., Lukk, A. A., & Kulagin, B. (1974). Block structure of the Earth's crust of Tadzhikistan. In *Searches for precursors of earthquakes in prediction polygons* (pp. 70–84). Moscow, Russian Federation (RUS): Nauka.
- Li, S., Mooney, W. D., & Fan, J. (2006). Crustal structure of mainland China from deep seismic sounding data. *Tectonophysics*, 420(1–2), 239–252. <https://doi.org/10.1016/J.TECTO.2006.01.026>

- Li, W., Chen, Y., Yuan, X., Schurr, B., Mechie, J., Oimahmadov, I., & Fu, B. (2018). Continental lithospheric subduction and intermediate-depth seismicity: Constraints from S-wave velocity structures in the Pamir and Hindu Kush. *Earth and Planetary Science Letters*, 482, 478–489. <https://doi.org/10.1016/j.epsl.2017.11.031>
- Li, X., Wei, D., Yuan, X., Kind, R., Kumar, P., & Zhou, H. (2011). Details of the doublet Moho structure beneath Lhasa, Tibet, obtained by comparison of P and S receiver functions. *Bulletin of the Seismological Society of America*, 101(3), 1259–1269. <https://doi.org/10.1785/0120100163>
- Mechie, J., & Kind, R. (2013). A model of the crust and mantle structure down to 700 km depth beneath the Lhasa to Golmud transect across the Tibetan Plateau as derived from seismological data. *Tectonophysics*, 606, 187–197. <https://doi.org/10.1016/j.tecto.2013.04.030>
- Mechie, J., Schurr, B., Yuan, X., Schneider, F., Sippl, C., Minaev, V., et al. (2019). Observations of guided waves from the Pamir seismic zone provide additional evidence for the existence of subducted continental lower crust. *Tectonophysics*, 762, 1–16. <https://doi.org/10.1016/j.tecto.2019.04.007>
- Mechie, J., Yuan, X., Schurr, B., Schneider, F., Sippl, C., Ratschbacher, L., et al. (2012). Crustal and uppermost mantle velocity structure along a profile across the Pamir and southern Tien Shan as derived from project TIPAGE wide-angle seismic data. *Geophysical Journal International*, 188(2), 385–407. <https://doi.org/10.1111/j.1365-246X.2011.05278.x>
- Molnar, P., & Bendick, R. (2019). Seismic moments of intermediate depth earthquakes beneath the Hindu Kush: Active stretching of a blob of sinking thickened mantle lithosphere? *Tectonics*, 38, 1651–1665. <https://doi.org/10.1029/2018TC005336>
- Molnar, P., & Stock, J. M. (2009). Slowing of India's convergence with Eurasia since 20 Ma and its implications for Tibetan mantle dynamics. *Tectonics*, 28, TC3001. <https://doi.org/10.1029/2008TC002271>
- Nábélek, J., Hetényi, G., Vergne, J., Sapkota, S., Kafle, B., Jiang, M., et al., & t. H.-C. Team (2009). Underplating in the Himalaya-Tibet collision zone revealed by the Hi-CLIMB experiment. *Science*, 325(5946), 1371–1374. <https://doi.org/10.1126/science.1167719>
- Najman, Y., Appel, E., Boudagher-Fadel, M., Bown, P., Carter, A., Garzanti, E., et al. (2010). Timing of India-Asia collision: Geological, biostratigraphic, and palaeomagnetic constraints. *Journal of Geophysical Research*, 115, B12416. <https://doi.org/10.1029/2010JB007673>
- Negredo, A. M., Replumaz, A., Villaseñor, A., & Guillot, S. (2007). Modeling the evolution of continental subduction processes in the Pamir-Hindu Kush region. *Earth and Planetary Science Letters*, 259(1-2), 212–225. <https://doi.org/10.1016/j.epsl.2007.04.043>
- Pavlis, G. L., & Das, S. (2000). The Pamir-Hindu Kush seismic zone as a strain marker for flow in the upper mantle. *Tectonics*, 19(1), 103–115. <https://doi.org/10.1029/1999TC900062>
- Pegler, G. L., & Das, S. (1998). An enhanced image of the Pamir-Hindu Kush seismic zone from relocated earthquake hypocentres. *Geophysical Journal International*, 134(2), 573–595. <https://doi.org/10.1046/j.1365-246x.1998.00582.x>
- Perry, M., Kakar, N., Ischuk, A., Metzger, S., Bendick, R., Molnar, P., & Mohadjer, S. (2019). Little geodetic evidence for localized Indian subduction in the Pamir Hindu Kush of Central Asia. *Geophysical Research Letters*, 46, 109–118. <https://doi.org/10.1029/2018GL080065>
- Peykre, Y. B., Pokhvisneva, Y. A., & Zotov, I. A. (1981). The Muskol metamorphic complex of the central Pamir. *International Geology Review*, 24, 297–303.
- Reguzzoni, M., Sampietro, D., & Sansò, F. (2013). Global Moho from the combination of the CRUST2.0 model and GOCE data. *Geophysical Journal International*, 195(1), 222–237. <https://doi.org/10.1093/gji/ggt247>
- Robert, A. M. M., Fernández, M., Jiménez-Munt, I., & Vergés, J. (2017). Lithospheric structures in central Eurasia derived from elevation, geoid anomaly and thermal analysis. *Geological Society of London, Special Publication*, 427(1), 271–293. <https://doi.org/10.1144/SP427.10>
- Robinson, A. C., Ducea, M., & Lapen, T. J. (2012). Detrital zircon and isotopic constraints on the crustal architecture and tectonic evolution of the northeastern Pamir. *Tectonics*, 31, TC2016. <https://doi.org/10.1029/2011TC003013>
- Robinson, A. C., Yin, A., Manning, C. E., Harrison, T. M., Zhang, S.-H., & Wang, X.-F. (2004). Tectonic evolution of the northeastern Pamir: Constraints from the northern portion of the Cenozoic Kongur Shan extensional system, western China. *Geological Society of America Bulletin*, 116(7), 953–973. <https://doi.org/10.1130/b25375.1>
- Roecker, S. W. (1982). Velocity structure of the Pamir-Hindu Kush region: Possible evidence of subducted crust. *Journal of Geophysical Research*, 87(B2), 945–959. <https://doi.org/10.1029/jb087ib02p00945>
- Rutte, D., Ratschbacher, L., Khan, J., Stübner, K., Hacker, B. R., Stearns, M. A., et al. (2017). Building the Pamir-Tibet Plateau-Crustal stacking, extensional collapse, and lateral extrusion in the Central Pamir: 2. Timing and rates. *Tectonics*, 36, 385–419. <https://doi.org/10.1002/TC004294>
- Rutte, D., Ratschbacher, L., Schneider, S., Stübner, K., Stearns, M. A., Gulzar, M. A., & Hacker, B. R. (2017). Building the Pamir-Tibet Plateau: Crustal stacking, extensional collapse, and lateral extrusion in the central Pamir: 1. Geometry and kinematics. *Tectonics*, 36, 342–384. <https://doi.org/10.1002/2016TC004293>
- Sass, P., Ritter, O., Ratschbacher, L., Tympel, J., Matiukov, V. E., Rybin, A. K., & Batalev, V. Y. (2014). Resistivity structure underneath the Pamir and southern Tian Shan. *Geophysical Journal International*, 198(1), 564–579. <https://doi.org/10.1093/gji/ggu146>
- Schmidt, J., Hacker, B. R., Ratschbacher, L., Stübner, K., Stearns, M., Kylander-Clark, A., et al. (2011). Cenozoic deep crust in the Pamir. *Earth and Planetary Science Letters*, 312(3-4), 411–421. <https://doi.org/10.1016/j.epsl.2011.10.034>
- Schneider, F. M., Yuan, X., Schurr, B., Mechie, J., Sippl, C., Haberland, C., et al. (2013). Seismic imaging of subducting continental lower crust beneath the Pamir. *Earth and Planetary Science Letters*, 375, 101–112. <https://doi.org/10.1016/j.epsl.2013.05.015>
- Schurr, B., Ratschbacher, L., Sippl, C., Gloaguen, R., Yuan, X., & Mechie, J. (2014). Seismotectonics of the Pamir. *Tectonics*, 33, 1501–1518. <https://doi.org/10.1002/2014TC003576>
- Schurr, B., Yuan, X., Haberland, C., Mechie, J., & Kufner, S.-K. (2012). TIPTIMON (Tien Shan-Pamir Monitoring Program) TAJIKISTAN (2012/2014). Deutsches GeoForschungsZentrum GFZ. Other/Seismic Network. <https://doi.org/10.14470/0P7567352807>
- Schurr, B., Yuan, X., Haberland, C., Mechie, J., & Kufner, S.-K. (2013). TIPTIMON (Tian Shan-Pamir Monitoring Program) AFGHANISTAN (2013/2014). Deutsches GeoForschungsZentrum GFZ. Other/Seismic Network. <https://doi.org/10.14470/1P7568352842>
- Schwab, M., Ratschbacher, L., Siebel, W., McWilliams, M., Minaev, V., Lutkov, V., et al. (2004). Assembly of the Pamirs: Age and origin of magmatic belts from the southern Tien Shan to the southern Pamirs and their relation to Tibet. *Tectonics*, 23, TC4002. <https://doi.org/10.1029/2003TC001583>
- Shaffer, M., Hacker, B. R., Ratschbacher, L., & Kylander-Clark, A. R. C. (2017). Foundering triggered by the collision of India and Asia captured in xenoliths. *Tectonics*, 36, 1913–1933. <https://doi.org/10.1002/2017TC004704>
- Sippl, C., Ratschbacher, L., Schurr, B., Krumbiegel, C., Rui, H., Pingren, L., & Abdybachev, U. (2014). The 2008 Nura earthquake sequence at the Pamir-Tian Shan collision zone, southern Kyrgyzstan. *Tectonics*, 33, 2382–2399. <https://doi.org/10.1002/2014TC003705>
- Sippl, C., Schurr, B., Tympel, J., Angiboust, S., Mechie, J., Yuan, X., et al. (2013). Deep burial of Asian continental crust beneath the Pamir imaged with local earthquake tomography. *Earth and Planetary Science Letters*, 384, 165–177. <https://doi.org/10.1016/j.epsl.2013.10.013>

- Sippl, C., Schurr, B., Yuan, X., Mechie, J., Schneider, F. M., Gadoev, M., et al. (2013). Geometry of the Pamir-Hindu Kush intermediate-depth earthquake zone from local seismic data. *Journal of Geophysical Research: Atmospheres*, *118*, 1438–1457. <https://doi.org/10.1002/jgrb.50128>
- Smith, W. H. F., & Wessel, P. (1990). Gridding with continuous curvature splines in tension. *Geophysics*, *55*(3), 293–305. <https://doi.org/10.1190/1.1442837>
- Stammler, K. (1993). Seismichandler—Programmable multichannel data handler for interactive and automatic processing of seismological analyses. *Computers & Geosciences*, *19*(2), 135–140. [https://doi.org/10.1016/0098-3004\(93\)90110-q](https://doi.org/10.1016/0098-3004(93)90110-q)
- Stearns, M. A., Hacker, B. R., Ratschbacher, L., Lee, J., Cottle, J. M., & Kylander-Clark, A. R. C. (2013). Synchronous Oligocene-Miocene metamorphism of the deep Pamir and Himalaya driven by plate-scale dynamics. *Geology*, *41*(10), 1071–1074. <https://doi.org/10.1130/G34451.1>
- Stearns, M. A., Hacker, B. R., Ratschbacher, L., Rutte, D., & Kylander-Clark, A. R. C. (2015). Titanite petrochronology of the Pamir gneiss domes: Implications for middle to deep crust exhumation and titanite closure to Pb and Zr diffusion. *Tectonics*, *34*, 784–802. <https://doi.org/10.1002/2014TC003774>
- Steffen, R., Steffen, H., & Jentzsch, G. (2011). A three-dimensional Moho depth model for the Tien Shan from EGM2008 gravity data. *Tectonics*, *30*, TC5019. <https://doi.org/10.1029/2011TC002886>
- Stübner, K., Ratschbacher, L., Rutte, D., Stanek, K., Minaev, V., Wiesinger, M., Gloaguen, R., & project TIPAGE members (2013). The giant Shakh dara migmatitic gneiss dome, Pamir, India-Asia collision zone: 1. Geometry and kinematics. *Tectonics*, *32*, 948–979. <https://doi.org/10.1002/tect.20057>
- Stübner, K., Ratschbacher, L., Weise, C., Chow, J., Hofmann, J., Khan, J., et al., & project TIPAGE Members (2013). The giant Shakh dara migmatitic gneiss dome, Pamir, India-Asia collision zone: 2. Timing of dome formation. *Tectonics*, *32*, 1404–1431. <https://doi.org/10.1002/tect.20059>
- Tian, X., & Zhang, Z. (2013). Bulk crustal properties in NE Tibet and their implications for deformation model. *Gondwana Research*, *24*(2), 548–559. <https://doi.org/10.1016/j.gr.2012.12.024>
- Wessel, P., & Smith, W. H. F. (1998). New, improved version of generic mapping tools released. *Eos, Transactions American Geophysical Union*, *79*(47), 579. <https://doi.org/10.1029/98EO00426>
- Xu, Q., Zhao, J., Yuan, X., Liu, H., & Pei, S. (2017). Detailed configuration of the underthrusting Indian lithosphere beneath western Tibet revealed by receiver function images. *Journal of Geophysical Research: Solid Earth*, *122*, 8257–8269. <https://doi.org/10.1002/2017JB014490>
- Yuan, X., Kind, R., Li, X., & Wang, R. (2006). The S receiver functions: Synthetics and data example. *Geophysical Journal International*, *165*(2), 555–564. <https://doi.org/10.1111/j.1365-246X.2006.02885.x>
- Yuan, X., Mechie, J., & Schurr, B. (2008). Tian Shan Pamir Geodynamics Project (TIPAGE). Deutsches GeoForschungsZentrum GFZ. Other/Seismic Network. <https://doi.org/10.14470/20097102>
- Yuan, X., Ni, J., Kind, R., Mechie, J., & Sandvol, E. (1997). Lithospheric and upper mantle structure of southern Tibet from a seismological passive source experiment. *Journal of Geophysical Research*, *102*(B12), 27,491–27,500. <https://doi.org/10.1029/97JB02379>
- Yuan, X., Sobolev, S. V., Kind, R., Oncken, O., Bock, G., Asch, G., et al. (2000). Subduction and collision processes in the Central Andes constrained by converted seismic phases. *Nature*, *408*(6815), 958–961. <https://doi.org/10.1038/35050073>
- Zandt, G., & Ammon, C. J. (1995). Continental crust composition constrained by measurements of crustal Poisson's ratio. *Nature*, *374*(6518), 152–154. <https://doi.org/10.1038/374152a0>
- Zhu, L. P., & Kanamori, H. (2000). Moho depth variation in Southern California from teleseismic receiver functions. *Journal of Geophysical Research*, *105*(B2), 2969–2980. <https://doi.org/10.1029/1999JB900322>
- Zubovich, A., Schöne, T., Metzger, S., Mosienko, O., Mukhamediev, S., Sharshabaev, A., & Zech, C. (2016). Tectonic interaction between the Pamir and Tien Shan observed by GPS. *Tectonics*, *35*, 283–292. <https://doi.org/10.1002/2015TC004055>